INTERFACE

Research

THE ROYAL SOCIETY
PUBLISHING

Form and function of the teleost lateral line revealed using three-dimensional imaging and computational fluid dynamics

Hendrik Herzog[1], Birgit Klein[1] and Alexander Ziegler[2]

[1]Institut für Zoologie, Rheinische Friedrich-Wilhelms-Universität Bonn, Poppelsdorfer Schloss, 53115 Bonn, Germany
[2]Institut für Evolutionsbiologie und Ökologie, Rheinische Friedrich-Wilhelms-Universität Bonn, An der Immenburg 1, 53121 Bonn, Germany

HH, 0000-0003-0693-3007; AZ, 0000-0002-7572-6872

Fishes sense weak water motion using the lateral line. Among the thousands of described fish species, this organ may differ in size, shape and distribution of individual mechanoreceptors or lateral line canals. The reasons for this diversity remain unclear, but are very likely related to habitat preferences. To better understand the performance of the organ in natural hydrodynamic surroundings, various three-dimensional imaging datasets of the cephalic lateral line were gathered using *Leuciscus idus* as representative freshwater teleost. These data are employed to simulate hydrodynamic phenomena around the head and within lateral line canals. The results show that changes in canal dimensions alter the absolute stimulation amplitudes, but have little effect on the relation between bulk water flow and higher frequency signals. By contrast, depressions in the skin known as epidermal pits reduce bulk flow stimulation and increase the ratio between higher-frequency signals and the background flow stimulus.

1. Introduction

The lateral line enables fishes and aquatic amphibians to perceive weak fluid motion [1–3]. This complex sensory organ is composed of small, highly sensitive mechanoreceptors known as neuromasts. In fishes, neuromasts are spread over the head, trunk and tail [4,5]. An individual mechanoreceptor is either located on the surface of the animal (superficial neuromast (SN)) or inside fluid-filled lateral line canals (canal neuromast (CN)) [6,7]. While SNs respond to the surrounding water's flow velocity, CNs are sensitive to fluid motion caused by pressure gradients between adjacent pores that connect lateral line canals to the surrounding water [8,9]. Fishes may use these local pressure gradients to detect nearby prey, while rheotactic behaviour involves estimation of the global flow direction [10,11].

Previous investigations of different fish species revealed a large diversity of lateral line morphologies, including significantly varying numbers of SNs and CNs as well as the presence of highly branching or reduced canal systems [7,12]. However, detailed investigations that would include the precise number, distribution, size, orientation and sensitivity of SNs and CNs or measurements of canal and pore diameters are available only for selected model species such as the goldfish (*Carassius auratus)* [4,13], rainbow trout (*Oncorhynchus mykiss*) [14], ruffe (*Gymnocephalus cernua*) [15], black prickleback (*Xiphister atropurpureus*) [16,17], banded astyanax (*Astyanax fasciatus*) [18,19], selected cichlid species [7,20,21], as well as the zebrafish (*Danio rerio*) [22–27] and its larval stages [28–30]. This relatively small number of species investigated limits the functional interpretation of specific lateral line morphologies [31]. Although the different anatomical characteristics of SNs and CNs are indicative of a functional specialization, quantifications of neuromasts among closely related fish species have surprisingly so far provided only weak

evidence for a correlation between lateral line morphology and habitat preferences [5,32].

Besides the fact that small-scale hydrodynamic conditions occurring in natural habitats can currently only be assumed to exist—based primarily on flow tank experiments or hydrological modelling [33,34]—the physical principles underlying lateral line morphology are conventionally analysed using sophisticated mathematical procedures or hydrodynamic experiments based on scaled models. Previous studies investigated local flow fields that surround swimming fishes [35], spatial noise suppression by complex lateral line systems [36], bulk water flow sensing [37], spatial integration by canal structures [38], detection of Kármán vortex streets [39], dipole source localization [40,41], as well as hydrodynamic imaging [42–45]. However, in order not to influence the results through the presence of a measuring probe such as a hydrophone or a hot-wire anemometer, the evaluation of parameters has to be performed by means of mathematical modelling. Unfortunately, hydrodynamic environments are complex and therefore hard to control under experimental conditions [46], and only limited data are currently available that would permit supplying computational models with exact geometries of a fish's surface, its lateral line canal structure, or the position and spatial orientation of individual neuromasts.

To address these issues, the present study for the first time employs three-dimensional (3D) reconstructions of the cephalic lateral line gathered using non-destructive imaging techniques. The anterior components of the lateral line constitute the most complex part of the organ [12,47] and are involved in the detection of energetically favourable conditions, localization of drifting food items, as well as determination of flow velocity and direction [7,12]. The present article is composed of two main sections: in the first part, novel 3D reconstructions of the cephalic lateral line are provided using the ide (*Leuciscus idus* Linnaeus, 1758) as a model organism, while the second part focuses on the application of computational fluid dynamics (CFD) by means of finite-element modelling (FEM) experiments that are based on a subset of the obtained 3D models.

A comprehensive set of imaging techniques, including photogrammetry, contrast-enhanced micro-computed tomography (μCT) and laser scanning, was used to non-destructively obtain 3D data on the external as well as internal anatomy of the fish [48–50]. Subsequent simulations based on virtual excitations of the cephalic lateral line resulted in novel insights into (i) pressure and flow fields induced by a vibrating sphere in bulk water flow, (ii) local flow velocity on the fish's surface, (iii) pressure amplitudes found near canal pores, (iv) flow velocity inside lateral line canals, and (v) hydrodynamic effects caused by the small-scale structuring of the fish's surface. The results are discussed in the light of recent studies of the teleost lateral line based on other forms of 3D models.

2. Material and methods

2.1. Experimental organisms
A total of eight specimens of the golden variety of the ide (Teleostei: Cyprinidae: *Leuciscus idus*) ranging from 6.3 to 16 cm total body length (TBL) were used for this study. The lateral line of the ide has previously been investigated using conventional techniques and the species is considered a generalist with regard to its lateral line morphology [32], i.e. the cephalic lateral line of the ide represents the basal organization found in most teleost fishes [12]. Living animals were obtained from a commercial dealer and were kept in an aquarium filled with 200 l of filtered freshwater.

2.2. Light microscopy
Vital staining using methylene blue (Sigma Aldrich M9140, 0.006% in 2 l of freshwater, incubation time 2 h) was performed on two specimens (7 and 7.5 cm TBL). The stained individuals were euthanized using an overdose of the fish anaesthetic tricaine mesylate (MS-222, Sigma Aldrich) and subsequently observed under a stereomicroscope (M8, Wild Heerbrugg AG) with a video camera (Moticam 1000, Motic) attached for documentation.

2.3. Photogrammetry
Two living specimens (15 and 16 cm TBL) were kept for 20 h in a methylene blue staining solution (0.006%) dissolved in 2 l of freshwater. Following staining, the fishes were euthanized using an overdose of MS-222 and decapitated. The heads were mounted vertically on a wooden plate using cotton wool and acrylic glue (Acrifix 192, Degussa) and the wooden plate was then glued to a structured rotating cone. Green paper was used to separate the background from the cone-mounted fish head. The scenery was illuminated using three spotlights and one gooseneck lamp. During rotation of the cone, 359 photographs (aperture 5.6, ISO 400, exposure 10 ms) were taken from four planes using a digital single-lens reflex camera (EOS 44D, Macro Lens EF 100 mm, Canon). The free software VISUALSFM [51] was used for feature detection [52], estimation of camera positions and bundle adjustment [53]. The resulting pixel cloud was transferred into a textured mesh using the free software MESHLAB (Visual Computing Lab, ISTI, CNR).

2.4. Micro-computed tomography
Two living specimens (6.3 and 7 cm TBL) were euthanized using an overdose of MS-222, fixed in 50 ml of a 4% paraformaldehyde (PFA) solution for 44 h and immersed in an ascending ethanol series (30% for 24 h, 50% for 24 h, 70% for 60 h; 300 ml each). To obtain soft tissue contrast, the specimens were transferred for 24 days to a staining solution of 70% ethanol containing 0.3% phosphotungstic acid (PTA, Merck). Subsequently, the specimens were transferred to a clean 70% ethanol solution for short-term storage. Shortly before scanning, each fish was placed in a 15 ml Falcon tube (Corning Inc.) filled with clean 70% ethanol. To avoid movement artefacts during scanning, specimens were fixed inside the tubes using small pieces of plastic. Scans of the head region were performed using μCT systems equipped with a 180 kV (phoenix v|tome|x s, General Electrics) and a 100 kV (SkyScan 1272, Bruker microCT) micro-focus X-ray tube. The scanning parameters on the v|tome|x s system were 130 kV source voltage, 170 μA source current, 667 ms exposure, 1200 frames acquired over 360° and 17 μm isotropic voxel resolution, while those on the SkyScan 1272 system were 70 kV source voltage, 142 μA source current, 2161 ms exposure, 1800 frames acquired over 180° and 5 μm isotropic voxel resolution. Reconstruction of the two scans to 16-bit tagged image file format (TIFF) image stacks was performed without compression using the software DATOSX Reconstruction on the v|tome|x s system and the software NRECON on the SkyScan 1272 system. Contrast enhancement of the image data and conversion to 8-bit TIFF stacks were performed using the free software IMAGEJ [54]. This program was also used for morphometric measurements. Manual segmentation of lateral line canals was performed

using the scan with 17 μm isotropic voxel resolution twice independently, once using the plug-in *Paint* of the free software Drishti [55] and once using the *Segmentation Editor* of the commercial software Amira v. 5.2 (FEI). The label fields resulting from each segmentation attempt were visually compared and found to be highly congruent.

2.5. Laser scanning

Two living specimens (10 and 10.5 cm TBL) were euthanized using an overdose of MS-222 and transferred into plastic tubes filled with 100 ml of tap water. PFA (8%) was slowly added (4 ml per 3 min, 100 ml in total) to fix the specimens in a PFA solution with a final concentration of 4%. The heads were removed and vertically mounted on a plastic board using acrylic glue and cotton wool. To reduce reflections, the surface of each head was coated with chalk spray (White colouring, Dupli-Color). A laser scanner with 35 μm spatial resolution (Edge ScanArm, FARO) was used to obtain a virtual 3D model of the surface. Finally, the commercial software Geomagic Wrap (3D Systems) was used to transform the resulting point cloud into a non-uniform rational b-splines (NURBS) model containing about 900 curved facets that was compatible with computer-aided design (CAD) software.

2.6. Three-dimensional reconstructions

The meshes derived from the photogrammetry, μCT and laser scanning experiments were further processed and optimized (mesh reduction, smoothing) using Meshlab and exported as virtual reality modelling language (VRML) files. These VRML files were then imported into the commercial software Adobe 3D Reviewer (Adobe Corporation) for further optimization (smoothing, colouring, labelling) and finally exported as interactive 3D portable document format (PDF) files following protocols described previously [56–58].

2.7. Computational fluid dynamics

The interaction of a virtual hydrodynamic surrounding with the fish's head was investigated using a laminar compressible flow model based on the Navier–Strokes equation in the commercial software Multiphysics 4.2 (COMSOL Inc.). This 3D CFD simulation incorporated results obtained during previous experiments [59,60]. According to these two studies, SNs and CNs differ in their capability to separate the hydrodynamic stimulation caused by bulk water flow directed from the snout to the rear of the fish and a small sphere vibrating parallel to the fish's midline. To this end, one of the 3D models gathered using laser scanning was virtually submerged into a cylinder (diameter 120 mm, height 65 mm) of water featuring laminar flow (velocity 10 cm s^{-1}) as well as a sphere (diameter 10 mm) vibrating close to the fish's eye (outline distance to fish 7 mm, sinusoidal displacements ± 2 μm, ± 10 μm, ± 50 μm and ± 150 μm at a vibration frequency of 50 Hz) (electronic supplementary material, figure S1a). In addition to the resulting flow velocity and pressure fields surrounding the vibrating sphere (electronic supplementary material, figure S1b), the flow velocity was measured close to the fish's surface at a distance of 50 μm (electronic supplementary material, figure S1d) [30]. To estimate the stimulation of the cephalic lateral line, pressure values were estimated at the locations where canal pores were present in the real fish (electronic supplementary material, figure S1c), and the pressure gradients along the canal segments were calculated by subtracting the pressure amplitudes found on adjacent pores. The stimulation of cephalic lateral line canals was approximated using a simplified tubular model (electronic supplementary material, figure S1e; diameters 39, 108 and 176 μm; length 1, 1.5 and 2 mm; estimated from μCT data), while the mesh of an isolated canal was derived from manual segmentation of the μCT data (electronic supplementary material, figure S1f). To investigate the influence of small pits located on the surface of the fish, a two-dimensional set-up featuring a water column and a skin section with pits of varying depth (10–450 μm) was used (electronic supplementary material, figure S1g). Fluid flow velocity was evaluated along the centre of the pit at a height of 0–1 mm as measured from the bottom of the pit. To visualize results derived from CFD experiments, looped video sequences were embedded into the electronic supplementary material using previously described protocols [58]. A comprehensive documentation of the simulation set-up is provided in the electronic supplementary material.

2.8. Data transparency

A MorphoBank project was created as a repository for digital raw data gathered in the course of this study. The tabs 'Media' and 'Documents' available on MorphoBank may be selected for online access to the deposited data [61].

3. Results

The cephalic lateral line of the ide was reconstructed in 3D using photogrammetry and μCT, while laser scanning was employed to obtain a virtual model of the shape of the fish's head. These structural data formed the basis for CFD studies of fluid motion around the fish's head and within lateral line canals.

3.1. Methodological considerations and morphological observations

Using photogrammetry, the shape and visual appearance of a methylene blue-stained fish head were reconstructed in 3D (figure 1). The underlying mesh of this model revealed only gross morphological features of the organism (figure 1; multimedia content in electronic supplementary material), while the photography-based texture information overlying the mesh conveyed a more plastic and detailed impression of the animal's anatomy. For example, the resolution of the photographic data was sufficient to visualize selected cephalic lateral line canals, side canals, larger canal pores, as well as individual CNs and SNs. Furthermore, these data revealed a high degree of bilateral symmetry of the entire cephalic lateral line system, although, as outlined below, this symmetry is not perfect.

A more detailed visualization of the external, but in addition also of the internal anatomy of the head of the ide was obtained using contrast-enhanced μCT (figure 2a). Virtual sagittal sections revealed that the contrast agent had penetrated a large variety of tissues, including epidermis, muscles, retina, gills and nerves, although diffusion of the contrast agent into some parts of the brain was not complete (figure 2b). In transverse sections, the cephalic lateral line canals were distinguishable from the remaining tissues as round or ellipsoid voids located within the mineralized skeleton (figure 2c). Lateral line canals were also identifiable in coronal sections (figure 2d).

Surface renderings based on the μCT dataset illustrate the almost perfect bilateral symmetry of the cephalic lateral line in this species (figure 3). However, distinct canal asymmetries, for example, at the junction of the infraorbital (IO) and otic (OT) or the preopercular (POP) and postotic (PO) canals became apparent (figure 3; multimedia content in electronic supplementary material). As a consequence of these
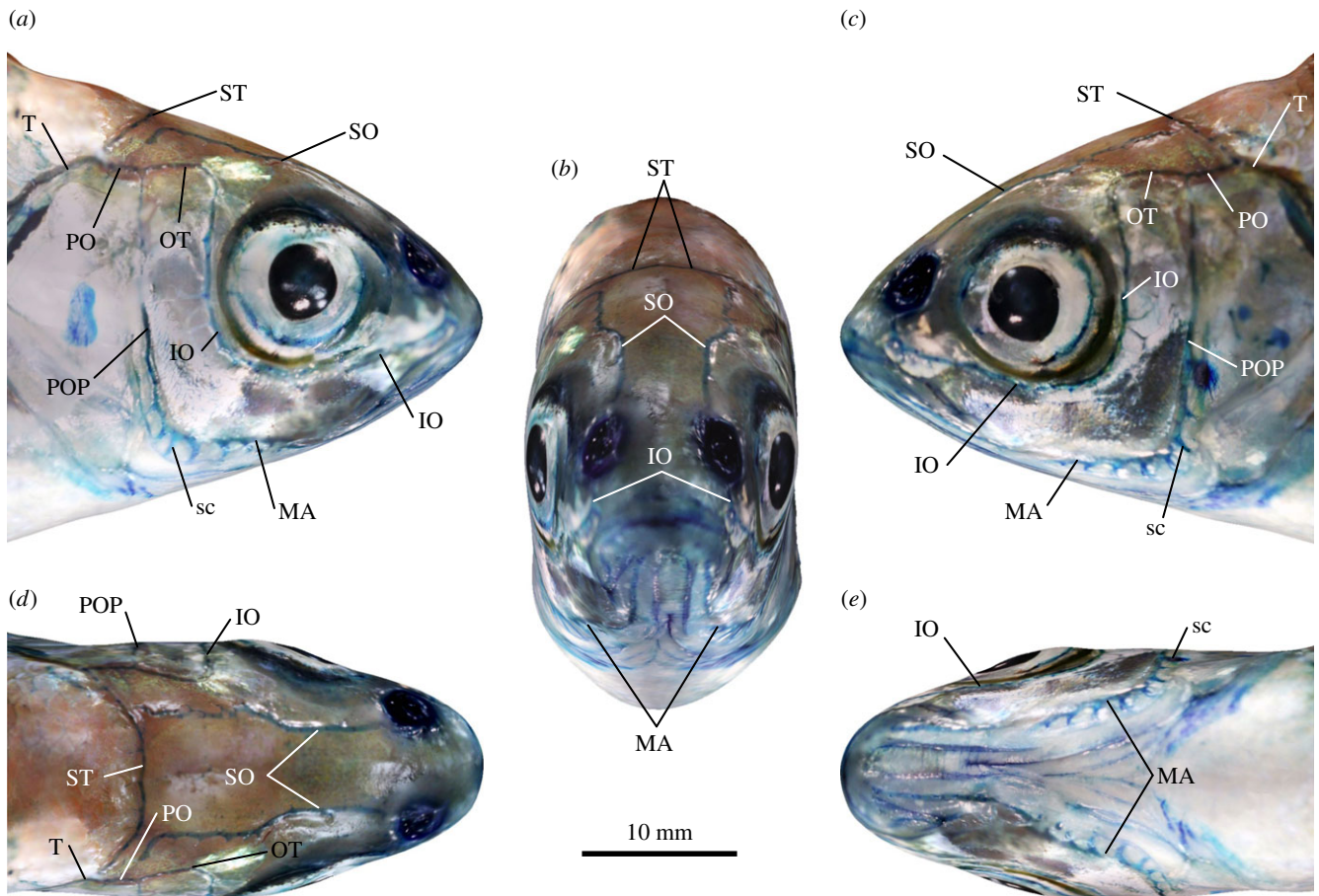
Figure 1. Morphology of the cephalic lateral line of *Leuciscus idus* analysed using photogrammetry. Structures were visualized using methylene blue staining. (*a*) Right lateral, (*b*) left lateral, (*c*) anterior, (*d*) dorsal and (*e*) ventral views. IO, infraorbital canal; MA, mandibular canal; OT, otic canal; PO, postotic canal; POP, preopercular canal; sc, side canal; SO, supraorbital canal; ST, supratemporal commissure; T, temporal canal.

asymmetries, the total number of canal pores found on the left and on the right side of the head differed slightly (electronic supplementary material, table S2). In the anterior part of the head, canal pores were located at comparable positions, while asymmetries became more pronounced in the posterior part. The contrast-enhanced µCT data also revealed the diameter of the corresponding canal pores. While side canals in general were short tubular structures that connected the main canal lumen to the water column through a single canal pore, side canals along the transition zone between the mandibular (MA) canal and the POP differed from this geometry. Here, these structures were present as elongated and proximally expanded canals (figure 3*b*,*c*,*e*).

The diameter of cephalic lateral line canals was first measured along nine equidistant planes (figure 3*b*). The supraorbital (SO) canal as well as the IO and MA had a mean diameter of 108 ± 27 µm, but varied distinctly within a range of 39–176 µm (electronic supplementary material, table S3). Additional measurements using the µCT dataset with 5 µm isotropic voxel resolution resulted in values between 73 and 187 µm, with a mean of 136 ± 28 µm. In addition to these measurements, reductions of the canal diameter to less than 25 µm were observed in the more posterior sections of the IO as well as in the dorsal sections of the POP (figure 3; multi-media content in electronic supplementary material). In general, a tendency in decrease of canal diameter from anterior to posterior was observed, particularly in case of the MA.

More detailed investigations of the µCT data (figure 4) revealed the presence of small hillock-shaped structures

($n = 7$) with dimensions of 137 ± 13 µm (length), 151 ± 19 µm (width) and 37 ± 4 µm (height) inside selected lateral line canals, in particular the supratemporal (ST) commissure (figure 4*b*). Based on their location, size and distribution, these structures were interpreted as CNs. In addition, small fluid-filled cavities adjacent to the main canal sections were found to be separated from the main canal lumen by a thin membrane (figure 4*c*). These elongated canals, here termed accessory cavities, were particularly prominent in the MA and POP.

SNs were not identified in the µCT datasets. However, using volume renderings with semi-transparent settings, depressions of the skeleton were found. These occurred primarily in the anterior region of the head, in particular above and below the eyes as well as close to the nostrils (figure 4*a*,*d*,*e*). These structures were not associated with lateral line canals and were located in areas that corresponded to those where clusters of SNs had been found using methylene blue-stained specimens (figure 4*f*). These depressions were therefore identified as epidermal pits, each of which represents a single pit organ [12]. In the anterior part of the head, the count of epidermal pits and SNs resulted in comparable numbers (electronic supplementary material, table S4). However, epidermal pits were only rarely observed in the posterior part of the head, although SNs were clearly identifiable in this region. A comparison of the number of epidermal pits and SNs present in different cephalic subsections revealed considerable differences, in particular on the operculum and below the eye. Measurements of epidermal
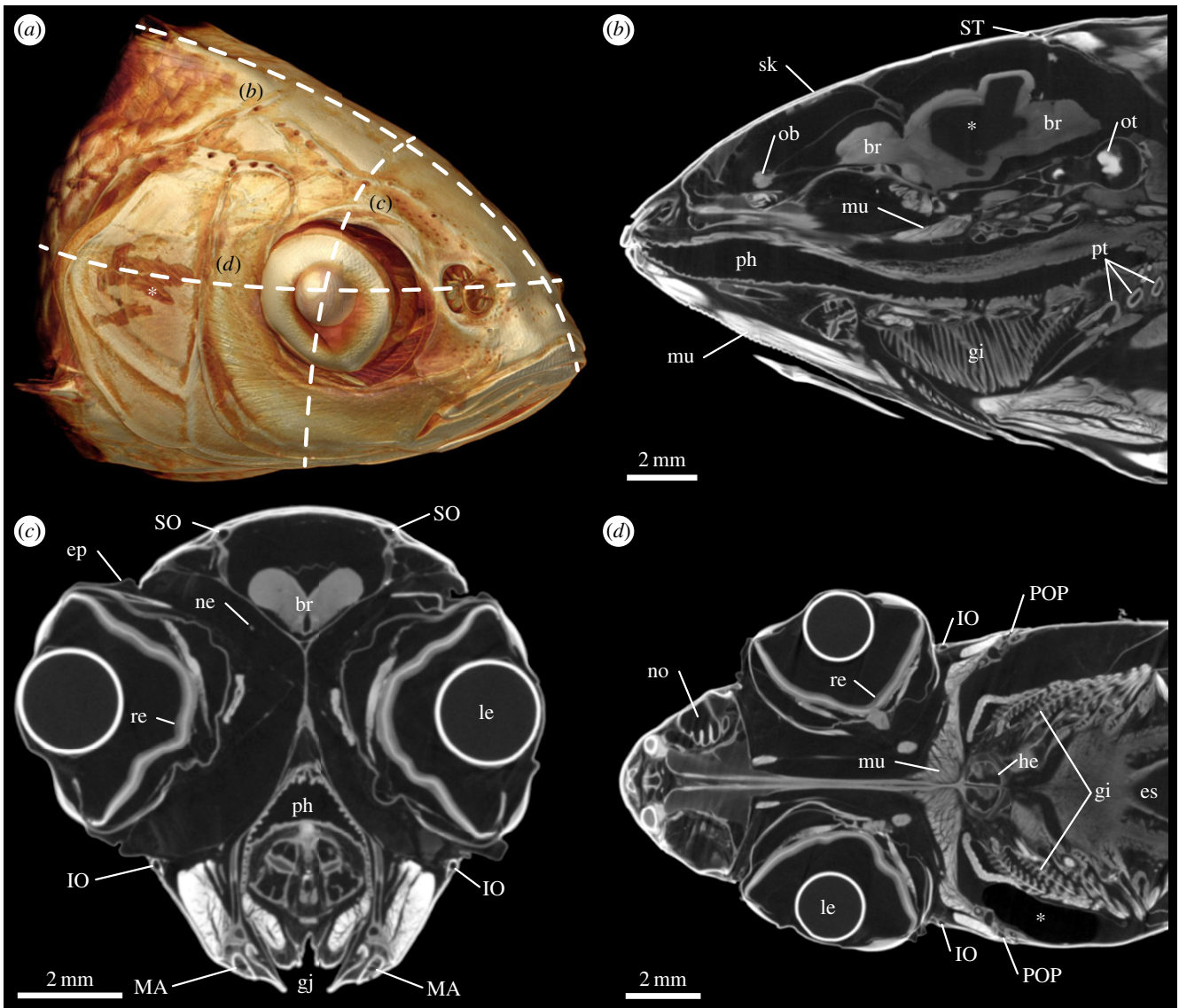
Figure 2. External and internal anatomy of the head of *Leuciscus idus* analysed using contrast-enhanced μCT. (*a*) Anterolateral view of a volume rendering illustrating the position of (*b*) sagittal, (*c*) transverse and (*d*) coronal virtual sections. Asterisk in (*a*) indicates a lesion of the skin caused during specimen handling. Asterisk in (*b*) depicts an area inside the brain with insufficient staining. Asterisk in (*d*) indicates a region with low X-ray absorption due to the presence of an air bubble. br, brain; ep, epithelium; es, oesophagus; gi, gill; gj, gill juncture; he, heart; IO, infraorbital canal; le, lens; MA, mandibular canal; mu, muscle tissue; ne, nerve tissue; no, nostril; ob, olfactory bulb; ot, otolith; ph, pharynx; POP, preopercular canal; pt, pharyngeal tooth; re, retina; sk, skeleton; SO, supraorbital canal; ST, supratemporal commissure.

pit dimensions along a dorsal and a lateral transect revealed that the epidermal pits varied in depth and width (electronic supplementary material, table S5). A comparison showed that deeper pits with, on average, smaller width were found in the dorsal part of the head. In addition, anterior–posterior gradients of pit dimensions were present in both transects, with anterior pits being deeper and broader.

Compared with the mesh data obtained using photogrammetry, the laser scanning experiments resulted in reconstructions of the fish's head with more detail (figure 5). Although larger structures like the eyes, gill covers, nostrils or the gill juncture were clearly visible in this model, smaller structures like individual scales were not so easily identifiable. However, due to the fact that the dense point cloud obtained using laser scanning resulted in a solid model with relatively few curved facets (figure 5; multimedia content in electronic supplementary material), this model was favoured for most of the subsequent CFD experiments.

3.2. Characterization of the principal stimuli for flow field simulations

The sphere vibrating in bulk water flow induced a characteristic flow and pressure signature in the water column of the virtual tank. This comprised a dipole-shaped alternating component originating from the vibrating sphere overlaid by a static component that was fitted by a sinusoidal function featuring an offset (electronic supplementary material). Figure 6*a* depicts the measuring points for these alternating current (AC) and direct current (DC) stimuli, respectively. For low vibration amplitudes, fluid flow in the surroundings of the vibrating sphere was dominated by the DC component. Here, the velocity was lowered upstream and downstream from the vibrating sphere, but was increased lateral to the sphere (figure 6*b*; multimedia content in electronic supplementary material). For high-vibration amplitudes, the DC component was modulated by the sinusoidal sphere
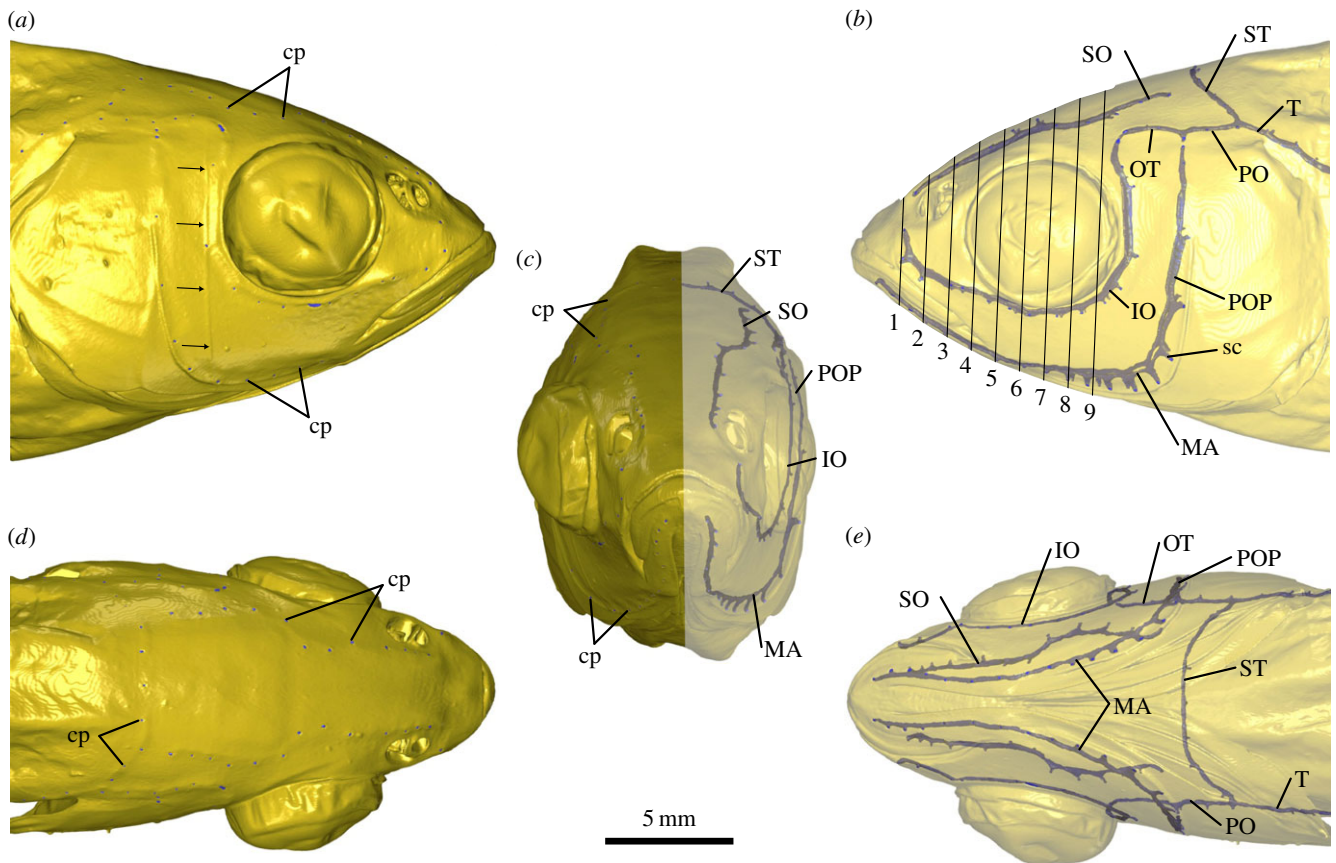
Figure 3. Three-dimensional visualization of the cephalic lateral line of *Leuciscus idus* based on contrast-enhanced μCT data. Individual canals were reconstructed using manual segmentation. (*a*) Right lateral, (*b*) left lateral, (*c*) anterior, (*d*) dorsal and (*e*) ventral views derived from shaded and semi-transparent surface renderings. Arrows in (*a*) indicate the results of a ring artefact present in the μCT dataset. Oblique lines in (*b*) indicate the planes at which canal diameters were measured (electronic supplementary material, table S3). cp, canal pore; IO, infraorbital canal; MA, mandibular canal; OT, otic canal; PO, postotic canal; POP, preopercular canal; sc, side canal; SO, supraorbital canal; ST, supratemporal commissure; T, temporal canal.

vibration, as shown in exemplary fashion for a sphere displacement of $\pm 50\,\mu m$ (figure 6*c*). With the exception of the downstream region that featured flow conditions similar to still water, the modulation of flow velocities induced by the vibrating sphere declined rapidly with increasing distance from the sphere (figure 7*a*; multimedia content in electronic supplementary material). The amplitudes of the sinusoidal pressure signatures also declined with increasing distance from the sphere, again shown exemplarily for a sphere displacement of $\pm 50\,\mu m$ (figure 6*d*). Because the static pressure was relatively small and declined with increasing distance from the sphere, the pressure signatures of the vibrating sphere were observed even at a distance of 7 mm along the vibrational axis (dark green curve in figure 6*d*). The relative signatures of the vibrating sphere exhibited characteristic spatial distributions, with the highest relative pressure signals found downstream (figure 7*b*). However, only weak flow signatures were present lateral to the sphere. In case of the modulated flow velocities, maximum values of the relative signal amplitudes were relatively low (dotted line in figure 7*c*). Correspondingly, the median values of the relative velocity signals from all measuring points were well below $-20\,dB$ (i.e. about 10%) for all vibration amplitudes. In contrast with this rather weak modulation of flow velocity, maximum values of the relative pressure signals were much higher (dotted line in figure 7*d*). An increase in the vibration amplitude from ± 2 to $\pm 150\,\mu m$ resulted in a systematic rise in the median values of all

measuring points from -20.3 to $+17.4\,dB$ (solid line in figure 7*d*). These results show that the vibrating sphere induced strong pressure signals that spread widely, but caused only low modulation of the bulk water flow in its immediate surroundings.

3.3. Simulation of the background stimulus for superficial neuromasts

Static flow velocities (i.e. the DC component) evaluated close to the fish surface ranged from 1.8 to $14.4\,mm\,s^{-1}$. For a $\pm 150\,\mu m$ sphere displacement amplitude, the modulation of the flow velocity (i.e. the AC component) caused by the vibrating sphere was in the range of $0.02{-}0.48\,mm\,s^{-1}$. The absolute modulation further decreased for lower vibration amplitudes with overall peak values of $0.18\,mm\,s^{-1}$ for $\pm 50\,\mu m$, $0.06\,mm\,s^{-1}$ for $\pm 10\,\mu m$ and $0.05\,mm\,s^{-1}$ for $\pm 2\,\mu m$ sphere displacement, while the relative velocity signal close to the fish's surface varied between individual measuring points (figure 8*a*). The corresponding pressure fields on the fish's surface are shown in figure 8*b* (multimedia content in electronic supplementary material). For a sphere displacement amplitude of $\pm 150\,\mu m$, the relative velocity signal ranged from -52.2 to $-18.5\,dB$ (figure 8*c*). However, for lower vibration amplitudes the relative velocity signal decreased with overall peak values of $-28.3\,dB$ for $\pm 50\,\mu m$, $-40.7\,dB$ for $\pm 10\,\mu m$ and $-41.3\,dB$ for $\pm 2\,\mu m$ sphere displacement. These findings illustrate that the
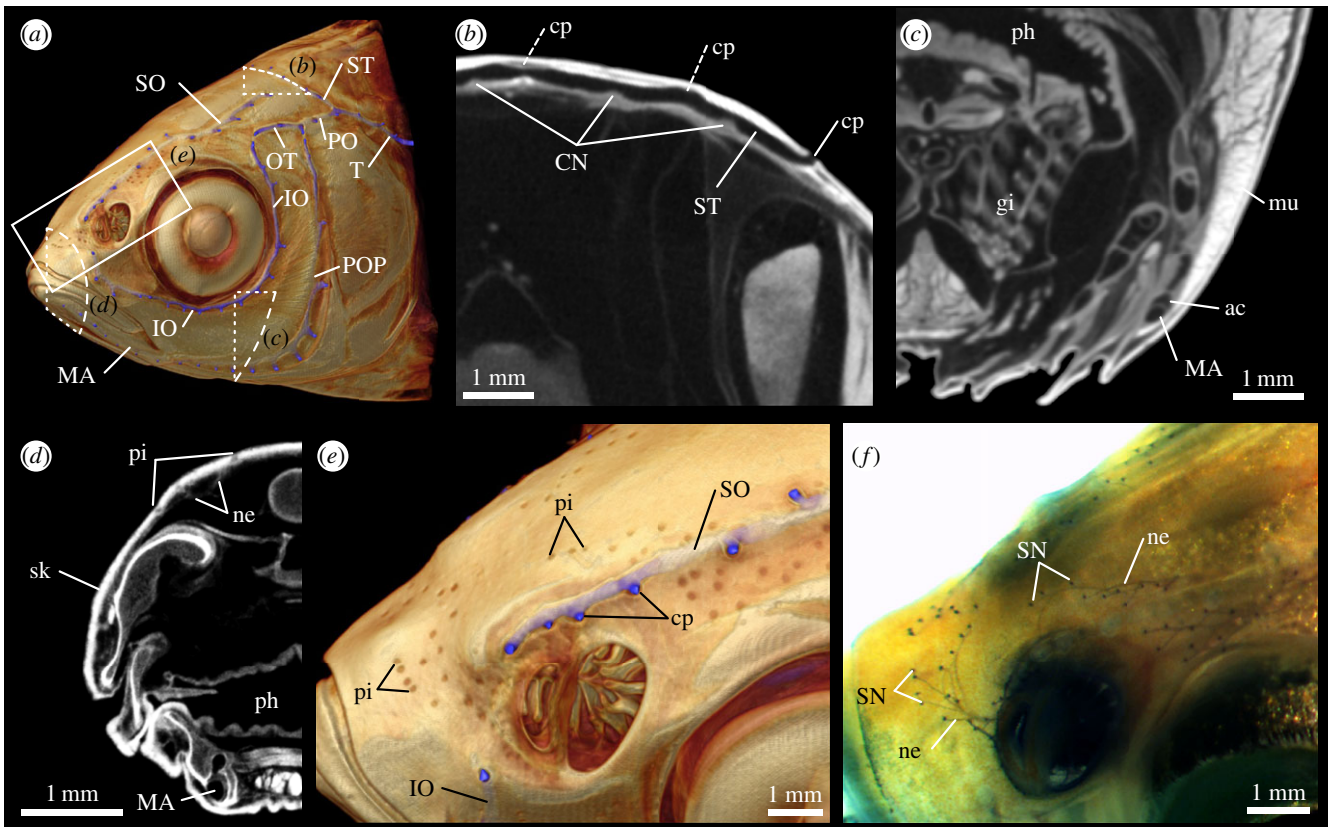
Figure 4. Detailed structure of the cephalic lateral line in *Leuciscus idus*. (*a*) Anterolateral view of a μCT-based, semi-transparent volume rendering showing the approximate positions of the following virtual sections and renderings. (*b*) Transverse section through the centre of the ST showing canal lumen, canal pores (two are only partly visible: dashed lines) and CNs. (*c*) Transverse section through the MA showing the accessory cavity adjacent to the canal. (*d*) Transverse section through the anterior part of the head showing afferent nerve fibres innervating SNs located in epidermal pits. (*e*) Close-up view showing the presence of several clusters of epidermal pits and their location relative to the left SO and IO. (*f*) Same view as shown in (*e*), but here based on a methylene blue-stained specimen showing the location of SNs. ac, accessory cavity; CN, canal neuromast; cp, canal pore; gi, gill; IO, infraorbital canal; MA, mandibular canal; mu, muscle tissue; ne, nerve tissue; ph, pharynx; pi, pit; POP, preopercular canal; SN, superficial neuromast; SO, supraorbital canal; ST, supratemporal commissure; T, temporal canal.
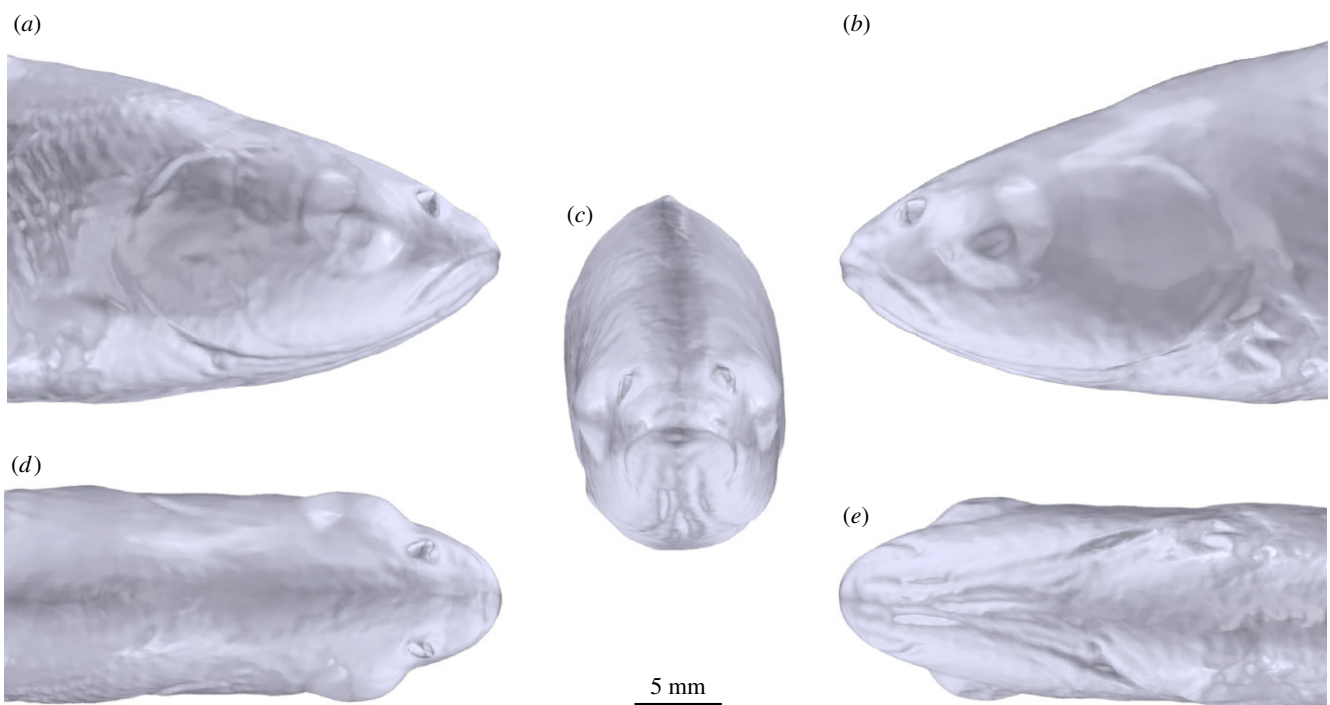

Figure 5. Morphology of the head of a specimen of *Leuciscus idus* analysed using laser scanning. (*a*) Right lateral, (*b*) left lateral, (*c*) anterior, (*d*) dorsal and (*e*) ventral views of a surface-rendered 3D model.
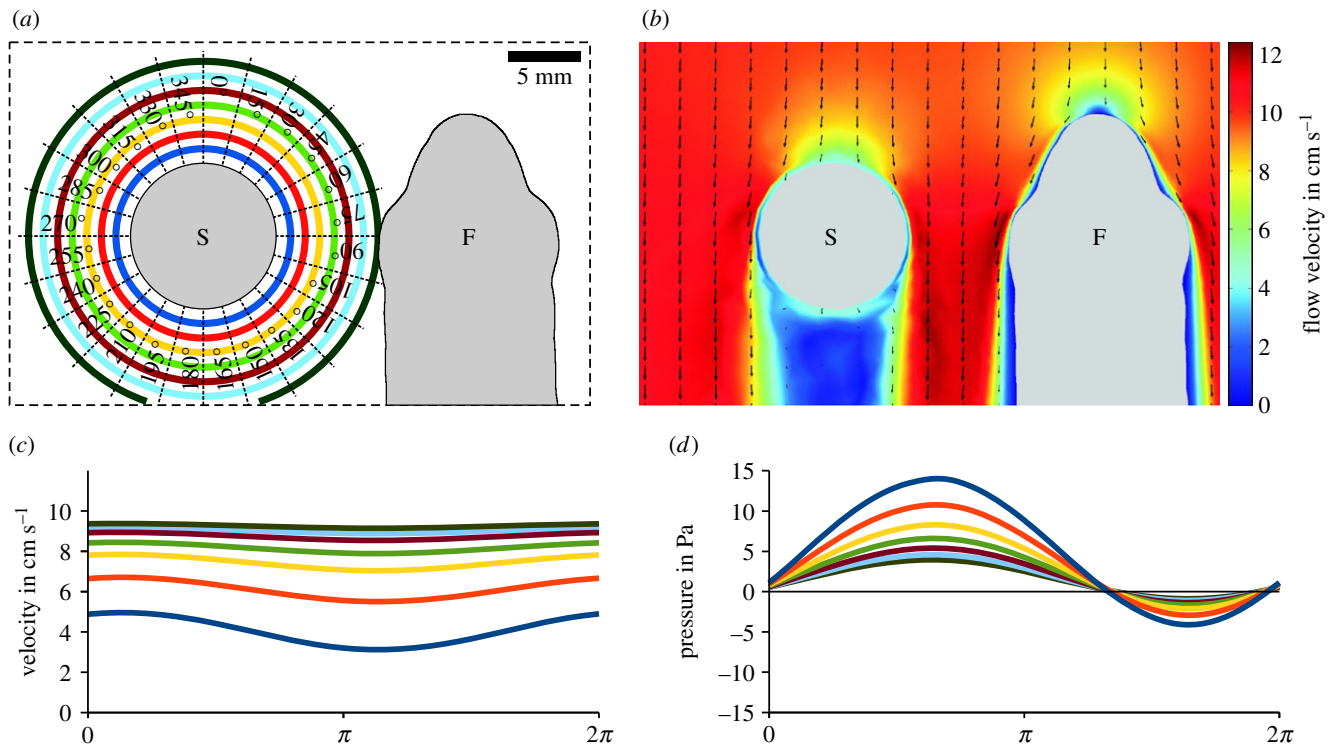
Figure 6. Simulation of bulk water flow and pressures induced by a vibrating sphere acting on the head of *Leuciscus idus*. (*a*) Dorsal view of the experimental set-up showing the vibrating sphere and a virtual section of the fish. The coloured rings refer to distances from the sphere (1–7 mm, step size 1 mm, 24 directions in steps of 15°). (*b*) Changes in the flow field within the bulk water flow (10 cm s⁻¹) induced by the vibrating sphere (amplitude ± 150 μm). Arrows show the direction of water flow, while the colour map indicates flow velocity magnitude. (*c,d*) Time course of the magnitude of the flow velocity (*c*) and pressure (*d*) along the main vibrational axis (0° in (*a*)) at distances of 1–7 mm for one cycle of sphere vibration (amplitude ± 50 μm). Note the vertical offsets of the sinusoidal signals. F, fish; S, sphere.

vibrating sphere modulated flow velocity close to the fish's surface only slightly, with the vibration signal being less than 1% of the local flow velocity induced by bulk water flow.

3.4. Stimulation of the cephalic lateral line

Static pressure gradients (i.e. the DC offset) that occurred along the canal segments (C) ranged from 5 mPa in C1 of the IO to 1021 mPa in C1 of the SO following a sphere displacement of ± 2 μm. For a sphere displacement amplitude of ± 150 μm, pressure gradient modulation induced by the vibrating sphere was widely spread between 25 and 1248 mPa. However, the absolute amplitude of the pressure gradient modulation decreased for lower vibration amplitudes with overall peak values of 415 mPa for ± 50 μm, 82 mPa for ± 10 μm and 18 mPa for ± 2 μm sphere displacement. For a ± 150 μm sphere displacement amplitude, relative difference pressure signals ranged from −27.1 to +30.3 dB. In general, smaller vibration amplitudes induced lower relative amplitudes in difference pressure with overall median values of −3.9 dB for ± 150 μm, −5.8 dB for ± 50 μm, −20.1 dB for ± 10 μm and −34.1 dB for ± 2 μm sphere displacement. These results show that, in contrast with the rather weak modulation of the local flow velocity, the vibrating sphere induced strong pressure differences along cephalic lateral line canals that measured up to 32.7 times the pressure gradients induced by bulk water flow. Therefore, pressure signals revealed sphere motion more prominently.

3.5. Simulation of fluid flow inside cephalic lateral line canals using a tubular model

In case of the simplified tubular model with dimensions that had been approximated based on the μCT data, a static difference pressure of 1 Pa (i.e. approximately the maximum induced by the bulk water flow) resulted in mean flow velocities of the canal fluid in a range of 4.7 μm s⁻¹ (diameter 39 μm, length 2 mm) to 193 μm s⁻¹ (diameter 174 μm, length 1 mm), with 48 μm s⁻¹ for the average size (diameter 108 μm, length 1.5 mm). The results of these simulations deviated by less than 2% from an analytical solution conducted using the Hagen–Poiseuille equation [61]. Canal fluid velocities for a sinusoidal 50 Hz signal of 100 mPa (i.e. 10% of the maximum pressure signal caused by bulk water flow) were in the range of 0.5–19.2 μm s⁻¹, with 4.8 μm s⁻¹ for the average size. However, the ratios between canal fluid velocities induced by alternating pressure signatures and bulk water flow were almost unaffected by tube size (−20.00 to −20.04 dB) and matched the ratio of the stimulus input of −20 dB. These findings indicate that filtering (of the 50 Hz alternating signal) induced by lateral line canals did not occur. Therefore, lateral line canals can detect static pressure gradients induced by bulk flow as well as alternating pressure gradients induced by a vibrating sphere.

3.6. Simulation of fluid flow inside cephalic lateral line canals using a realistic model

To better approximate fluid flow inside cephalic lateral line canals during the presence of bulk water flow and a vibrating
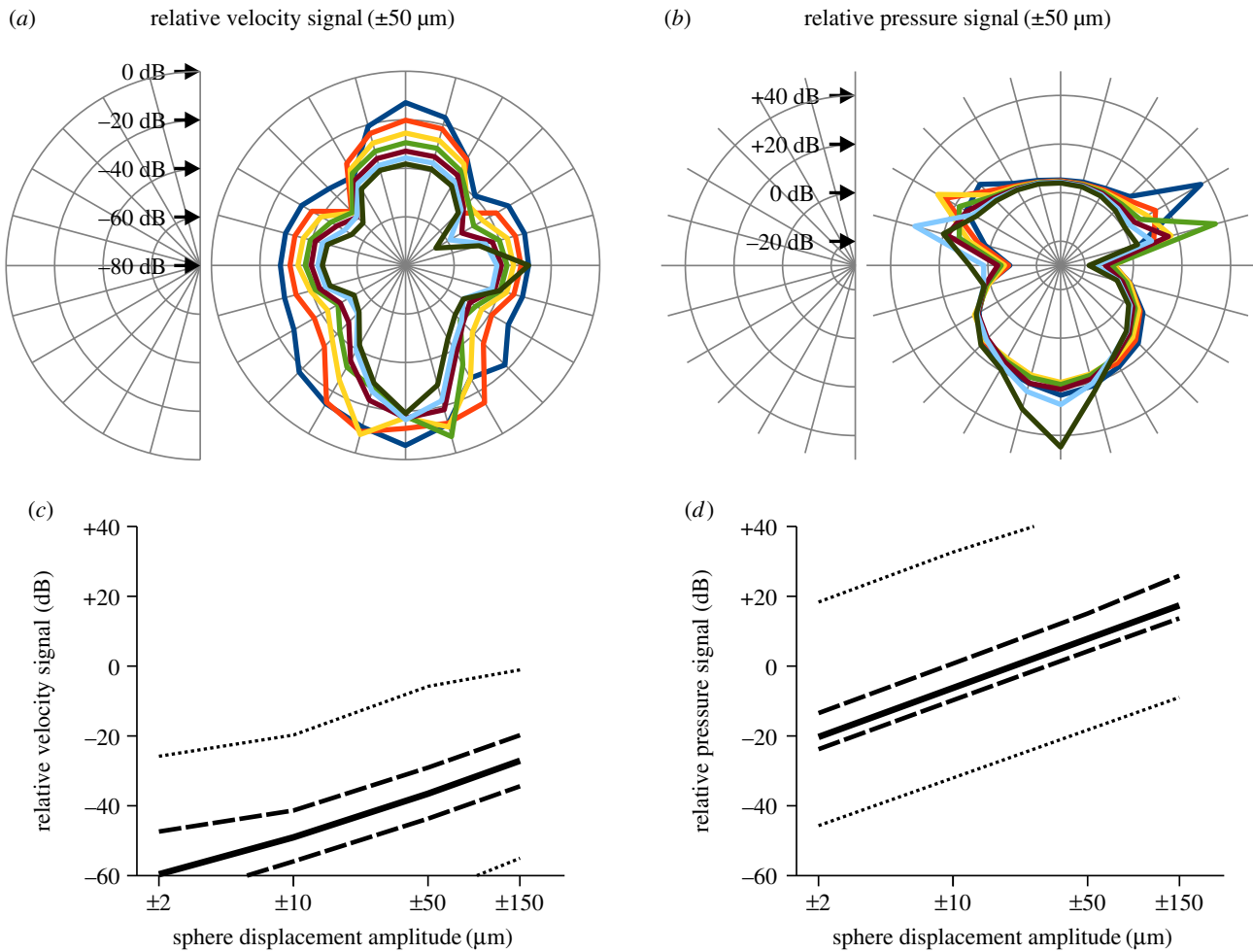
Figure 7. Spatial distribution and relative amplitude of flow and pressure fields induced by a sphere vibrating in bulk water flow. (a,b) The relative vibration signatures (displacement $\pm$ 50 μm) in velocity (a) and pressure (b) referenced to bulk water flow (10 cm s^{-1}) are shown as polar plots. Colour scheme and angles refer to figure 6a. Note that scaling between (a) and (b) differs by 50 dB. (c,d) Relative vibration signatures in velocity (c) and pressure (d) induced by sphere displacements of $\pm$ 2 μm, $\pm$ 10 μm, $\pm$ 50 μm and $\pm$ 150 μm. Plots show the median (solid line), 1st/3rd quartile (dashed lines) and minimum/maximum (dotted lines) values obtained from measuring points depicted in figure 6a.

sphere, the same pressures acting on the virtual measuring points placed on the fish's head (figure 8a) were applied to all 13 canal pores (P) of an isolated canal, the right SO (figure 9). The static component of the pressure gradients was strongest in the anterior part of the canal between the first four pores (figure 9a) and resulted in DC flow velocities in C1–C3 of 46–124 μm s^{-1} (figure 9b). By contrast, C4–C12 elicited lower canal fluid velocities of 1–19.4 μm s^{-1}. However, sphere vibration induced flow velocities of up to 60 μm s^{-1}. The relative sphere signals varied widely between −51.8 and +25.1 dB (figure 9c). C1 showed the lowest and C10 the highest relative sphere signals. These results show that bulk water flow induces a relatively strong DC signal in the most anterior canal segments. However, sphere vibration can still be detected by means of CNs located in the more posterior canal segments.

3.7. Effects of epidermal pit dimensions on local flow velocity

Simulations of the effects of epidermal pits (figure 4d,e) on local flow fields showed a significant reduction in bulk water flow velocities inside these depressions (figure 10a). However, this effect was observable only up to a pit

depth of about 270 μm (figure 10b). Once this depth was exceeded, a reversal in flow direction was observed that led to an increase in flow velocities inside the pit (figure 10a; multimedia content in electronic supplementary material). Although the position of a measuring point that was shifted from 10 to 150 μm above the bottom of the pit had little influence on this effect, absolute values of the estimated velocities varied with the position of the measuring point (figure 10c). When a sinusoidal velocity signal was superimposed on a constant flow stimulus, the DC component of the signal was more strongly attenuated by an increase in pit depth than by higher-frequency components (figure 10d). As a consequence, the relative velocity signal of the higher frequency signals increased for deeper pits up to a depth of about 350 μm (figure 10e). As indicated by the vertical offset in the 25, 50, 100 and 200 Hz curves, the attenuation of local fluid flow by epidermal pits is dependent on stimulus frequency (figure 10e). These findings demonstrate that small-scale structural modifications can have a strong influence on local flow fields with respect to frequency filtering and absolute amplitude. The epidermal pits are likely to reduce local flow velocity and thus prevent excessive stimulation of SNs by bulk water flow.
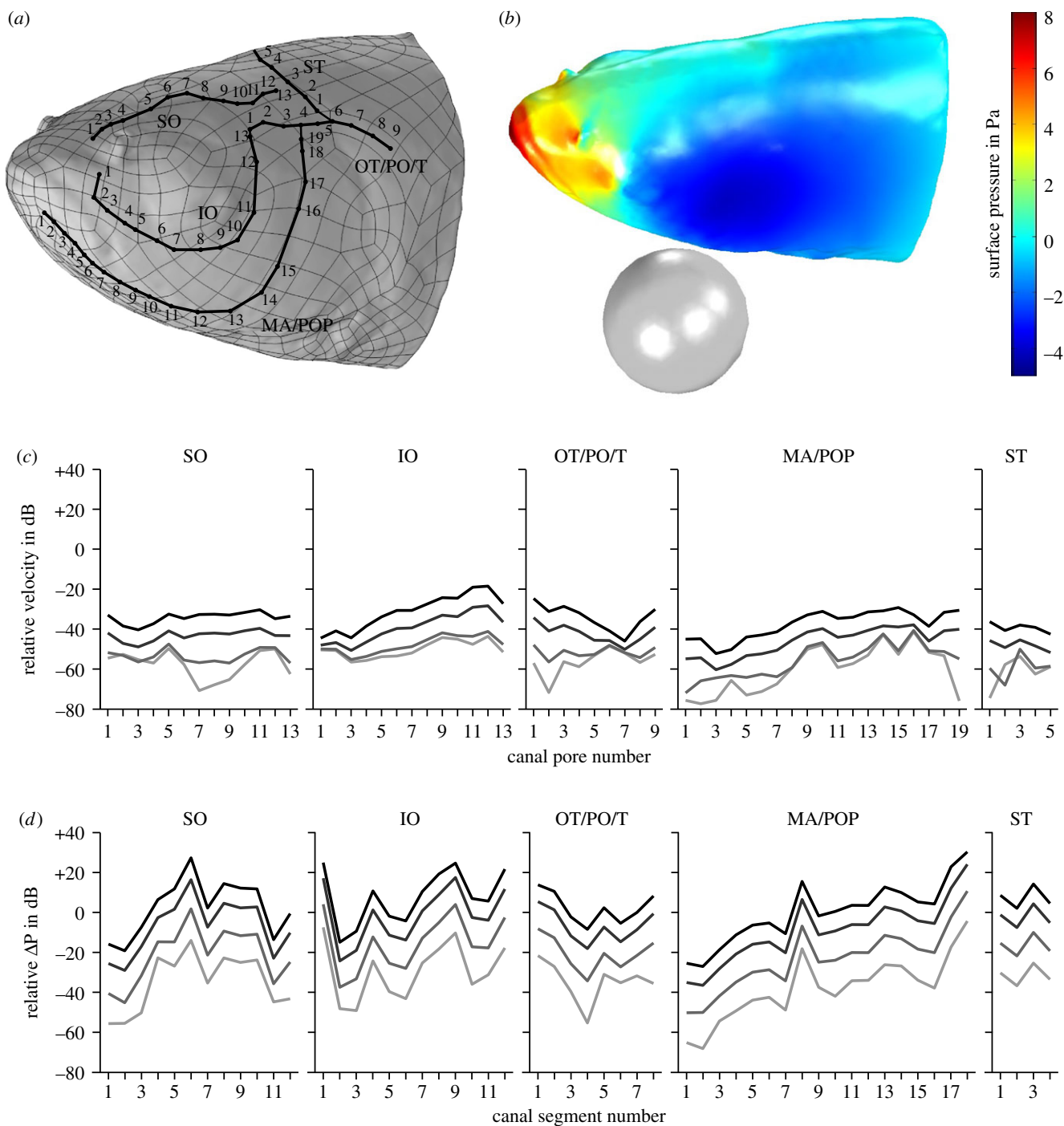
Figure 8. Simulation of the pressure induced by a vibrating sphere and bulk water flow (10 cm s^{-1}) on head and canal pores of *Leuciscus idus*. (*a*) Left lateral view of the laser scanning-based model featuring vertices, cephalic lateral line canals and manually placed measuring points (numbered black dots). (*b*) Exemplary pressure field on the surface of the fish's head induced by a sphere vibrating parallel to the fish with an amplitude of $\pm$ 150 μm in bulk water flow. (*c,d*) Relative flow velocity close to the fish's surface near the canal pore (*c*) and relative pressure gradients along canal segments (*d*). The location of the measuring points is provided in (*a*). Lines denote displacement amplitudes of $\pm$ 150 μm (black), $\pm$ 50 μm (dark grey), $\pm$ 10 μm (grey) and $\pm$ 2 μm (light grey). IO, infraorbital canal; MA, mandibular canal; OT, otic canal; PO, postotic canal; POP, preopercular canal; SO, supraorbital canal; ST, supratemporal commissure; T, temporal canal.

4. Discussion

The lateral line is a complex organ composed of a diverse array of mineralized and soft tissues [6,7]. Some of its constituent parts are present on the fish's surface (SNs), some are located within or below the epidermis (pit organs), while others are embedded into the skeleton (lateral line canals, CNs). To successfully visualize this complex set of tissues, complementary imaging techniques had to be employed.

4.1. Photogrammetry-based reconstructions of the cephalic lateral line

Using photogrammetry, the 3D shape of the head was not resolved with much detail, as illustrated by the low complexity of the mesh (figure 1; multimedia content in electronic supplementary material). However, the overlying texture data provide all the morphological information commonly revealed by methylene blue staining, such as the course of lateral line canals or the distribution of SNs and CNs. In the
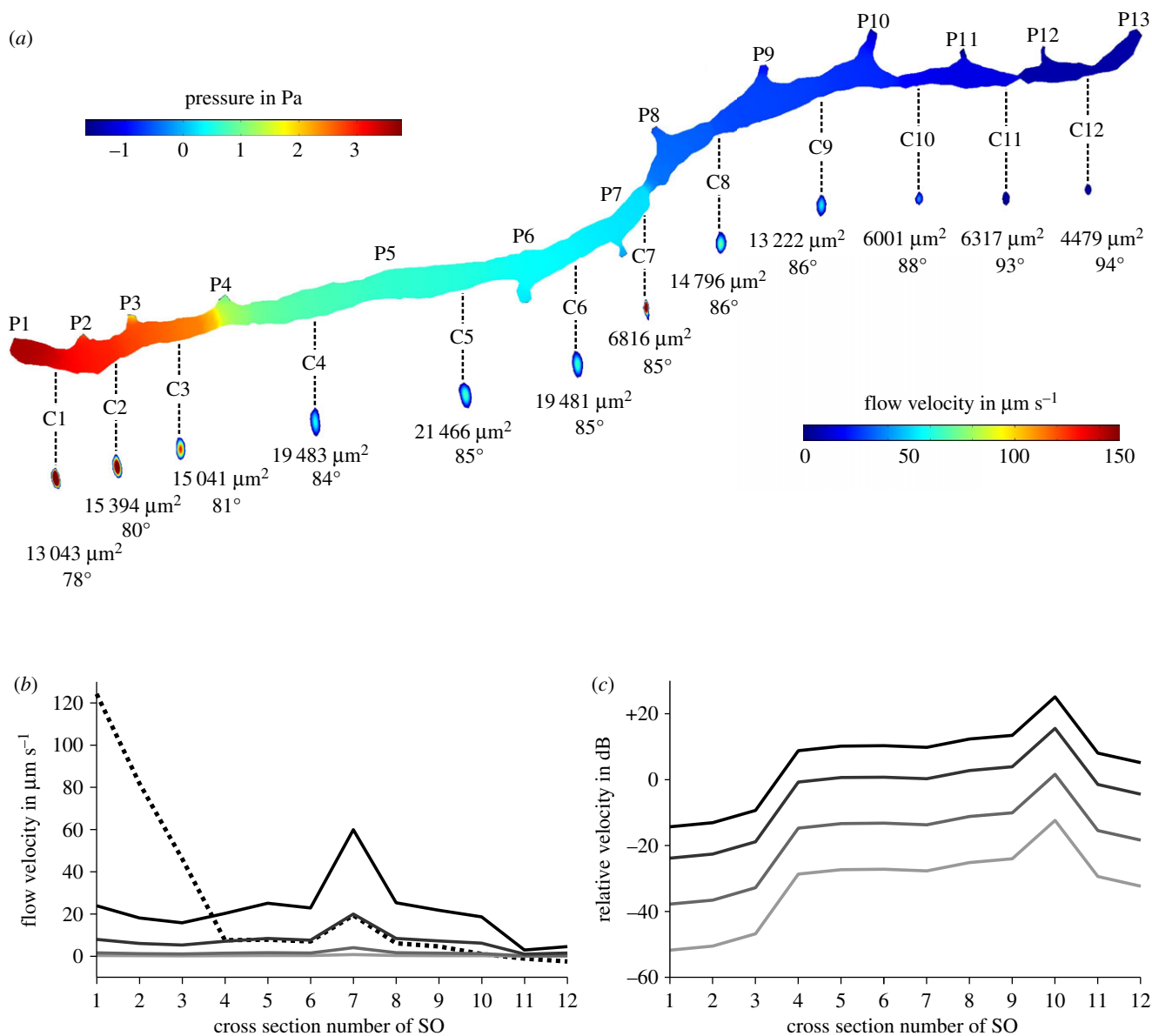
Figure 9. Simulation of fluid flow inside the right supraorbital canal (SO) of *Leuciscus idus*. (a) Pressure on the canal walls and fluid flow velocity induced by pressures acting on the canal pores caused by bulk flow and a vibrating sphere. Numbers below the cross sections provide the area of the respective cross section as well as the phase of the sine wave. (b) Average flow velocity of canal fluid measured along the cross sections shown in (a) for DC (dashed line) and sphere displacements of $\pm 150\ \mu m$ (black), $\pm 50\ \mu m$ (dark grey), $\pm 10\ \mu m$ (grey) and $\pm 2\ \mu m$ (light grey). (c) Relative amplitudes of sphere signal for displacements of $\pm 150\ \mu m$ (black), $\pm 50\ \mu m$ (dark grey), $\pm 10\ \mu m$ (grey) and $\pm 2\ \mu m$ (light grey) referred to DC flow velocity induced by bulk water flow. C1–C12, canal segment 1–12; P1–P13, canal pore 1–13.

context of the present study, photogrammetry thus was indispensable for evaluating 3D data additionally acquired using μCT and laser scanning. However, in some parts the photogrammetry-based reconstruction showed a significant degree of blurring and misalignment of the texture, in particular near the snout and on the gill covers. These areas were characterized by reflective surfaces, which may have complicated both the generation of the mesh and that of a detailed texture. Although it would require a more complex experimental set-up, such reflections can be reduced by immersion of the organism in water and subsequent underwater photography.

Previous studies used methylene blue, but also other stains such as fluorescence markers to investigate selected components of the lateral line [26,62–64]. However, photogrammetric reconstructions depend on the presence of edge-like features that can be used for the estimation of the camera positions as well as the creation of the pixel cloud

based on triangulation. Therefore, it seems unlikely that photogrammetry will be carried out using fishes treated with such advanced staining protocols. A further disadvantage of photogrammetry is that the precise spatial data required for morphometric analyses cannot be acquired due to triangulation mismatches that are likely to occur during reconstruction of the pixel cloud. Despite these drawbacks, photogrammetry of methylene blue-stained fishes in combination with interactive 3D modelling as carried out here constitutes a relatively straightforward, low-cost way to rapidly document the structural diversity of the lateral line in multiple species.

4.2. Contrast-enhanced micro-computed tomography of the cephalic lateral line

μCT has previously been used to investigate the morphology of cephalic lateral line canals among different fish species
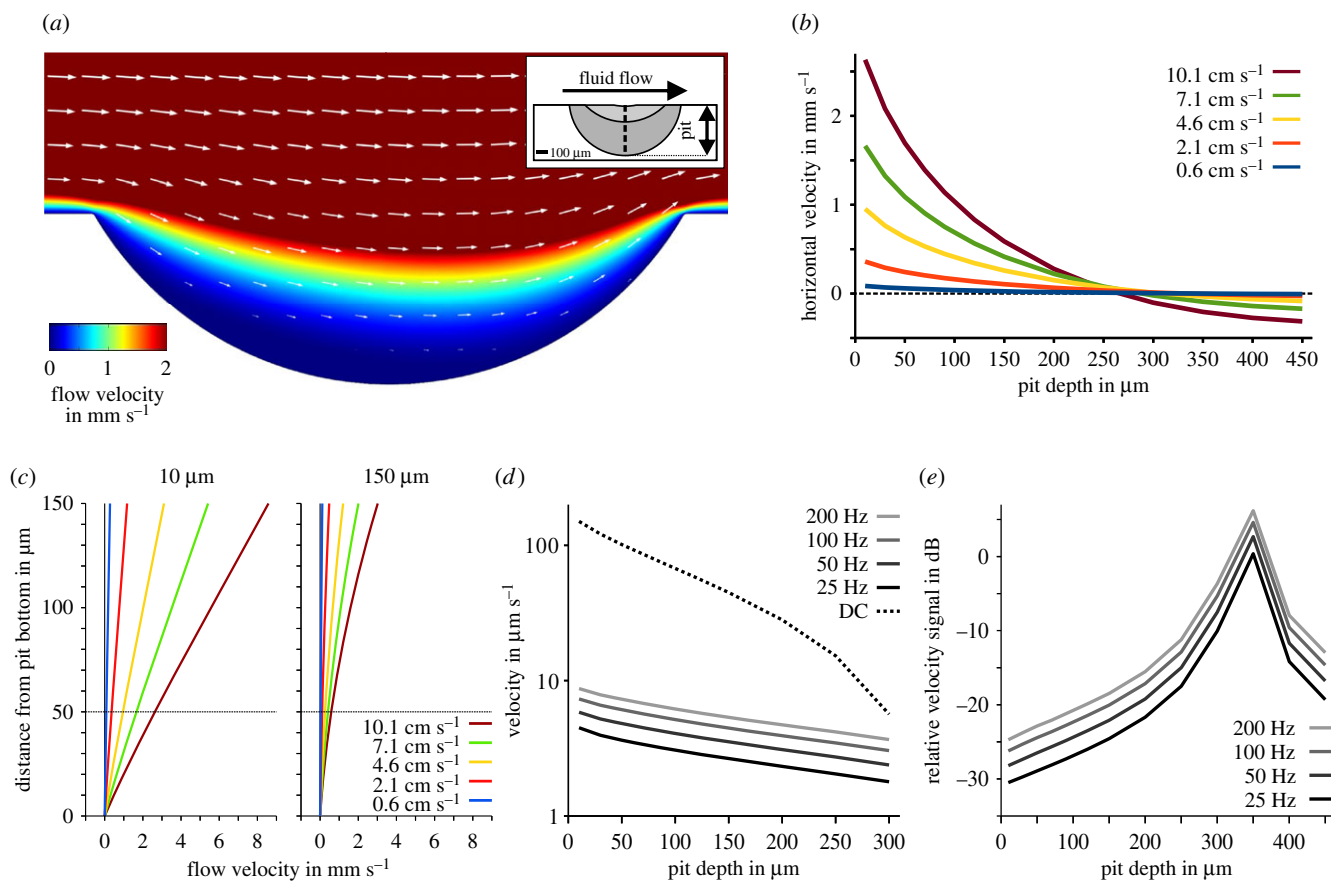
Figure 10. Influence of epidermal pits on surface hydrodynamics of *Leuciscus idus*. (*a*) Exemplary flow field induced by a DC flow of 10 cm s^{-1} and a pit depth of 150 μm (velocity magnitude colour-coded, arrows pointing in the direction of flow, arrow lengths scaled logarithmically). (*b*) Horizontal flow velocity magnitude at 50 μm above the bottom of the pit for various pit depths and bulk flow velocities. (*c*) Horizontal flow velocity magnitude above the pit bottom for various bulk flow velocities used for stimulation. The two images show exemplary velocity profiles at 0–150 μm distance from the pit bottom for pit depths of 10 μm (left) and 150 μm (right). (*d*) Absolute flow velocity (logarithmic scaling) at a distance of 50 μm from the bottom of the pit for bulk water flow (DC, 10 mm s^{-1}, dashed black line), sinusoidal velocity amplitudes of 0.01 mm s^{-1}, and frequencies of 25 Hz (black line), 50 Hz (dark grey line), 100 Hz (grey line) and 200 Hz (light grey line). (*e*) Relative velocity amplitude of altering velocity signals of 25 Hz (black line), 50 Hz (dark grey line), 100 Hz (grey line) and 200 Hz (light grey line) as referred to the DC signal (dashed line shown in (*d*)).

[7,21,65]. Although these studies resulted in detailed information on mineralized structures, μCT scans of unstained specimens usually provide little insight into the soft part anatomy of complex organs. Although magnetic resonance imaging (MRI) is highly suitable to depict soft parts in fishes [66], MRI-inherent artefacts at tissue boundaries [67] as well as relatively low isotropic voxel resolutions [68] render this technique inadequate for imaging lateral line canals. However, results obtained using μCT in combination with contrast-enhanced specimens of the orange chromide (*Etroplus maculatus*), spotted seatrout (*Cynoscion nebulosus*), red drum (*Sciaenops ocellatus*) and Norfolk spot (*Leiostomus xanthurus*) suggested that this approach might be useful for the simultaneous non-destructive visualization of lateral line hard and soft parts at sufficient resolution [49,50]. Although previous studies had used iodine to stain fishes, PTA was chosen here due to its improved tissue-staining properties [48,69]. Despite the relatively low diffusion rate of this contrast agent, penetration of the samples after 3.5 weeks was almost complete (figure 2).

The isotropic voxel resolution of the initially obtained μCT scan (i.e. 17 μm) was adequate for the unambiguous identification of lateral line canals and various other components of the organ. Although specific anatomical aspects such as epidermal pits or individual nerves were more visible

in the subsequently made scan with 5 μm isotropic voxel resolution (figure 4*d*), the first dataset was chosen for manual segmentation due to hardware limitations. The morphometric measurements revealed distinct variations of the diameter of lateral line canals. As the simulations using a tubular and a realistic canal model revealed, such morphological variation can influence the local velocity of the canal fluid. This result emphasizes the importance of small-scale variations in the complex 3D structure of lateral line canals. However, some deviations between evaluations using the two scans became apparent. Most probably, these differences can be attributed to the fact that the angular orientation and position of the measured sections differed slightly.

In general, the μCT data had excellent signal-to-noise ratio (figure 2). However, several artefacts were observed that were either related to the scanning protocol (ring artefact shown in figure 3*a*) or to handling and fixation of the specimens, for example lesions of the skin (figure 2*a*) or unnaturally protruding eyeballs (figure 2*c*). However, these locally constrained artefacts did not have any influence on the results presented here. A further element of bias, i.e. the process of manual segmentation was compensated for by conducting segmentation independently by two individuals [70].

The interactive 3D model of the cephalic lateral line canals with their side canals and canal pores (figure 3; multimedia

content in electronic supplementary material) can be used to illustrate the high degree of bilateral symmetry that these structures display. In contrast with the previously made observation of an incomplete formation of the ST [32], the ST in our specimens connects both with the left and the right temporal (T) canal. Furthermore, and in agreement with the previous finding that the POP has no connection with the OT [32], large constrictions within particular canals resulting in canal diameters of less than 25 µm were observed in the posterior-most sections of the POP and IO. The spatial relation and dimensions of individual canal pores and segments were investigated in detail and showed a characteristic arrangement with slight variations (figure 3). Most probably, the variability in spatial orientation of the canal pores and canal cross sections reflects adaptations to hydrodynamic conditions on a small-scale level. In addition, the µCT scans revealed small fluid-filled cavities adjacent to the MA (figure 4c), whose detailed structure and function are currently unknown.

CNs were only found in sections of specific cephalic lateral line canals, in particular the ST (figure 4b). These hillock-shaped structures were identified as CNs based on their shape, size and location in between two adjacent pores (figure 4b). The surprisingly rare occurrence of CNs in the µCT data could be related to the high length-to-width ratio of these structures [21,71]. In the ide, the size of an individual CN was estimated to be about 23×104 µm [32]. In contrast with these structures, SNs could not be identified in the µCT scans due to their small dimensions of about 20×50 µm in the ide [32]. However, SN size varies considerably among the different fish species analysed thus far [27,47,71,72]. Surprisingly, the scan with 5 µm isotropic voxel resolution also did not reveal the presence of any SNs. Thus, it seems unlikely that the absence of SNs in the present µCT data is a result of inadequate resolution alone, but could also be related to the fixation or staining protocols employed. However, as previous investigations with conventional techniques have shown [2], the epidermal pits identified on the surface of the fish's head (figure 4d–f) accurately reflect positions where SNs are located.

4.3. Laser scanning of the head of the ide

Owing to the fact that the application of high-resolution µCT datasets in CFD simulations can be hampered by software or hardware limitations, laser scanning was here used to generate a less complex 3D model of the head of the ide. A disadvantage of laser scanning is that this technique gathers information only about the surface characteristics of a sample. Because lateral line canals are usually submerged into the skin or skeleton of fishes, they are not accessible for analysis using this approach. Furthermore, surface structures such as SNs or canal pores are relatively small and easily concealed by chalk spray that had to be used for reduction of surface reflections. The laser scanning model was thus found to be best suited for CFD experiments involving the entire head. However, as the simulation data demonstrate, these relatively simple measurements of flow and pressure fields surrounding the head of a fish can reveal a considerable amount of valuable information. These data were further augmented by adding information on canal diameters and the position of canal pores that had been gathered using the other two 3D imaging techniques (electronic supplementary material).

4.4. Computational fluid dynamics of the cephalic lateral line

At first, CFD experiments were used to investigate how flow velocity and pressure signatures generated by a small vibrating sphere interact with an additionally presented background stimulus. In case of the alternating signatures of the vibrating sphere, the simulations revealed spatial pressure and velocity distributions that had previously been predicted based on theoretical work as well as experimental data [8,40].

In comparison to the reference values based on equations proposed for 'ideal dipoles' [73], the pressure amplitudes elicited by the vibrating sphere (distance 5 mm, direction $0°$) were about 7% larger (± 2 µm: 0.13 Pa = +7.4%; ± 10 µm: 0.63 Pa = +7.5%; ± 50 µm: 3.16 Pa = +7.1%; ± 150 µm: 9.48 Pa = +6.8%). However, the present simulations featured, in contrast with theoretical calculations, the entire fish head, a limited tank volume and an additional bulk water flow. Such a more complex experimental set-up could explain the observed deviations in pressure amplitudes.

Nonetheless, 3D FEM simulations are prone to quickly reach hardware limitations. For a vibration frequency of 50 Hz, the approximated thickness of the oscillatory boundary layers surrounding the fish head and vibrating sphere was calculated to be about 80 µm [41,73]. The element size in our simulation exceeded both the boundary layer and the measuring points at a distance of 50 µm from the fish's surface. As a consequence, these values were interpolated linearly based on larger mesh elements. In addition, complex boundary layer effects were not directly considered in this particular 3D simulation. Although these effects may become crucial in case of high-frequency signals, previous analytical solutions [27] demonstrate almost linear flow profiles at low frequencies such as the 50 Hz alternating signal used in the present simulation. For the low-frequency vibrations commonly used in previous studies, the boundary layer has only a minor effect on signal amplitudes [41]. In addition, it was previously shown that, for low-frequency signals, boundary layers can be neglected for both SNs and CNs [40]. These authors also showed that, for an incompressible fluid such as water, pressures acting perpendicular to the boundary layer are almost constant, so that the boundary layer does not play a role in case of hydrodynamic signals caused by a small sphere vibrating at low frequency. Another important hydrodynamic aspect that became apparent is that the fish surface is curved and features small depressions (i.e. the epidermal pits). Correspondingly, previous analytical approaches based on the flat plate theory [27,41] are unlikely to comprehensively reflect the hydrodynamics close to the fish's surface.

However, some mesh-induced effects became apparent in our 3D simulations, e.g. in the velocity downstream from the sphere (figure 6b; multimedia content in electronic supplementary material). In addition, the incomplete decline of relative signals by reduced sphere displacement amplitudes (figure 8c) indicates a limited resolution of low velocity values or additional hydrodynamic phenomena such as Kármán vortex streets downstream from the sphere [61]. A considerable increase of element numbers in the simulations could presumably help to reduce these effects, but will certainly also increase the amount of computational resources required.

As a consequence of the bulk water flow, velocity amplitudes of 1.8–14.4 mm s^{-1} were measured close to the fish's

surface, values well above previously estimated SN detection thresholds of 25–60 μm s^{-1} [73]. Although the velocity signatures of the vibrating sphere were much smaller—only about -20 dB (i.e. 10%) for the largest sphere displacement amplitude—these AC signals might still modulate the neuronal discharge pattern of nerve fibres already stimulated by bulk water flow. In addition, the complex cupula mechanics of SNs and CNs may result in a relevant amplification of higher frequencies [73]. However, for most measuring points and lower displacement amplitudes, the ratio between the vibration signature and the bulk water flow exceeded the typical dynamic range of SNs of about 40 dB [74]. Moreover, even small fluctuations in flow velocity may further decrease the signal-to-noise ratio for AC signatures and bulk water flow [59,60].

The pressure gradients along the cephalic lateral line canals induced by the vibrating sphere (i.e. up to 1.3 Pa) and bulk water flow (i.e. up to 1 Pa) resulted in median values of relative (AC/DC) difference pressure signatures ranging from 2% (-34.1 dB for $\pm 2\ \mu$m) to 156.7% ($+3.9$ dB for $\pm 150\ \mu$m). These pressure gradients were above the detection threshold of about 100 mPa calculated using previously published equations [73] as well as data on the cephalic lateral line of the ide (diameter 108 μm, length 1.5 mm per canal segment, CN detection threshold 5 μm s^{-1}), but most probably also match the typical dynamic range of CNs.

As these results demonstrate, flow velocity close to the vibrating sphere is only slightly modulated, while alternating pressure signatures are spreading widely and are the dominant feature to detect the vibrating sphere. Thus, a functional specialization of the two subsets of mechanoreceptors—with CNs responding to pressure gradients and SNs to flow velocity—is the only suitable explanation for the results obtained here as well as in previous studies [59,60]. These investigations help to explain why the cephalic lateral line plays such a dominant role in behavioural tasks of fishes [75].

However, a clear separation into SNs that code for bulk water flow and CNs that code for higher-frequency signals could be softened by small structural features present in the ide. As the morphological investigations carried out here have shown, SNs, particularly in the anterior part of the head, are located in small depressions. Although the actual dimensions of epidermal pits in larger specimens currently remain unknown, it seems reasonable to predict that pit depth in a specimen of about 30–40 cm TBL will be about 100–300 μm. Our results indicate that the functional meaning of the epidermal pits is a local extension of the boundary layer thickness, thereby inducing an attenuation of the DC component of bulk water flow [27,76–78]. As a consequence, epidermal pits reduce the high velocities found close to smooth surfaces once fishes are exposed to strong currents.

The velocities are reduced into a range more suitable for the dynamic range of SNs, thereby also avoiding mechanical damage to these sensitive mechanoreceptors. However, rapidly changing fluid flow, like that derived from nearby prey or predators, is attenuated much less. Therefore, the ratio between AC signals and the DC background flow can be increased by means of DC blocking induced by an extension of the boundary layer. An increase of about 10–30 dB is likely to be obtained by the epidermal pits.

As was previously shown [78], variations in lateral line canal dimensions have a strong influence on the velocity of canal fluids. In comparison to the low detection threshold (0.1–1 mPa) determined for the ruffe [73], the relatively small diameter of the cephalic lateral line canals of the ide (108 μm on average) leads to about 40–60 dB less sensitivity. The ruffe has large lateral line canals with an average diameter of 1 mm. By contrast, the relative velocity amplitudes of the 50 Hz vibration referred to the bulk flow stimulation were only slightly affected by these strong differences in canal dimensions: the geometry of the lateral line canals of the ide results in little attenuation of high-frequency hydrodynamic signals compared with canals featuring larger dimensions, a finding that is in agreement with theoretical work [79].

In conclusion, the epidermal pits present in the anterior part of the head of the ide as well as the, on average, relatively small diameter of this species' cephalic lateral line canals constitute morphological adaptations to a rheophilic life style. These structures reduce the stimulation of the cephalic lateral line by bulk water flow and enable this species to detect hydrodynamic signals of prey or approaching predators even in the presence of strong background currents.

References

1. Dijkgraaf S. 1933 Untersuchungen über die Funktion der Seitenorgane an Fischen. *Z. Physiol.* **20**, 162–214. (doi:10.1007/bf00340757)

2. Dijkgraaf S. 1962 The functioning and significance of the lateral-line organs. *Biol. Rev.* **38**, 51–105. (doi:10.1111/j.1469-185X.1963.tb00654.x)

3. Bleckmann H. 2008 Peripheral and central processing of lateral line information. *J. Comp. Physiol. A* **194**, 145–158. (doi:10.1007/s00359-007-0282-2)

4. Schmitz A, Bleckmann H, Mogdans J. 2008 Organization of the superficial neuromast system in goldfish, *Carassius auratus*. *J. Morphol.* **269**, 751–761. (doi:10.1002/jmor.10621)

5. Beckmann M, Erös T, Schmitz A, Bleckmann H. 2010 Number and distribution of superficial neuromasts in twelve common European cypriniform fishes and their relationship to habitat occurrence. *Int. Rev. Hydrobiol.* **95**, 273–284. (doi:10.1002/iroh.200911185)

6. Coombs S, Görner P, Münz H. 1989 *The mechanosensory lateral line: neurobiology and evolution*, 725 p. New York, NY: Springer.

7. Webb JF. 2013 Morphological diversity, development, and evolution of the mechanosensory

lateral line system. In *The lateral line system* (eds S Coombs, H Bleckmann, RR Fay, AN Popper), pp. 17–72. New York, NY: Springer.

8. Kalmijn A. 1988 Hydrodynamic and acoustic field detection. In *Sensory biology of aquatic animals* (eds J Atema, RR Fay, AN Popper, WN Tavolga), pp. 151–186. New York, NY: Springer.

9. Kroese ABA, Schellart NAM. 1992 Velocity- and acceleration-sensitive units in the trunk lateral line of the trout. *J. Neurophysiol.* **68**, 2212–2221.

10. Montgomery JC, Baker CF, Carton AG. 1997 The lateral line can mediate rheotaxis in fish. *Nature* **389**, 960–963. (doi:10.1038/40135)

11. Kanter MJ, Coombs S. 2003 Rheotaxis and prey detection in uniform currents by Lake Michigan mottled sculpin (*Cottus bairdi*). *J. Exp. Biol.* **206**, 59–70. (doi:10.1242/jeb.00056)

12. Coombs S, Janssen J, Webb J. 1988 Diversity of lateral line systems: evolutionary and functional considerations. In *Sensory biology of aquatic animals* (eds J Atema, RR Fay, AN Popper, WN Tavolga), pp. 553–593. New York, NY: Springer.

13. Puzdrowski RL. 1989 Peripheral distribution and central projections of the lateral-line nerves in goldfish, *Carassius auratus* (part 1 of 2). *Brain Behav. Evol.* **34**, 110–120. (doi:10.1159/000316066)

14. Montgomery JC, McDonald F, Baker CF, Carton AG, Ling N. 2003 Sensory integration in the hydrodynamic world of rainbow trout. *Proc. R. Soc. Lond. B* **270**, 195–197. (doi:10.1098/rsbl.2003.0052)

15. van Netten SM. 1991 Hydrodynamics of the excitation of the cupula in the fish canal lateral line. *J. Acoust. Soc. Am.* **89**, 310–319. (doi:10.1121/1.400512)

16. Bleckmann H, Münz H. 1990 Physiology of lateral-line mechanoreceptors in a teleost with highly branched, multiple lateral lines. *Brain Behav. Evol.* **35**, 240–250. (doi:10.1159/000115870)

17. Klein AT, Münz H, Bleckmann H. 2013 The functional significance of lateral line canal morphology on the trunk of the marine teleost *Xiphister atropurpureus* (Stichaeidae). *J. Comp. Physiol. A* **199**, 735–749. (doi:10.1007/s00359-013-0834-6)

18. Teyke T. 1990 Morphological differences in neuromasts of the blind cave fish *Astyanax hubbsi* and the sighted river fish *Astyanax mexicanus*. *Brain Behav. Evol.* **35**, 23–30. (doi:10.1159/000115853)

19. Baker CF, Montgomery JC. 1999 The sensory basis of rheotaxis in the blind mexican cave fish, *Astyanax fasciatus*. *J. Comp. Physiol. A* **184**, 519–527. (doi:10.1007/s003590050351)

20. Tarby ML, Webb JF. 2003 Development of the supraorbital and mandibular lateral line canals in the cichlid, *Archocentrus nigrofasciatus*. *J. Morphol.* **255**, 44–57. (doi:10.1002/jmor.10045)

21. Webb JF, Bird NC, Carter L, Dickson J. 2014 Comparative development and evolution of two lateral line phenotypes in Lake Malawi cichlids. *J. Morphol.* **275**, 678–692. (doi:10.1002/jmor.20247)

22. Metcalfe WK, Kimmel CB, Schabtach E. 1985 Anatomy of the posterior lateral line system in young larvae of the zebrafish. *J. Comp. Neurol.* **233**, 377–389. (doi:10.1002/cne.902330307)

23. Metcalfe WK. 1989 Organization and development of the zebrafish posterior lateral line. In *The mechanosensory lateral line* (eds S Coombs, P Görner, H Münz), pp. 147–159. Heidelberg, Berlin: Springer.

24. Webb JF, Shirey JE. 2003 Postembryonic development of the cranial lateral line canals and neuromasts in zebrafish. *Dev. Dynam.* **228**, 370–385. (doi:10.1002/dvdy.10385)

25. Ghysen A, Dambly-Chaudière C. 2004 Development of the zebrafish lateral line. *Curr. Opin. Neurobiol.* **14**, 67–73. (doi:10.1016/j.conb.2004.01.012)

26. Ghysen A, Dambly-Chaudière C. 2007 The lateral line microcosmos. *Gene. Dev.* **21**, 2118–2130. (doi:10.1101/gad.1568407)

27. McHenry MJ, Strother JA, van Netten SM. 2008 Mechanical filtering by the boundary layer and fluid-structure interaction in the superficial neuromast of the fish lateral line system. *J. Comp. Physiol. A* **194**, 795–810. (doi:10.1007/s00359-008-0350-2)

28. van Trump WJ, McHenry MJ. 2008 The morphology and mechanical sensitivity of lateral line receptors in zebrafish larvae (*Danio rerio*). *J. Exp. Biol.* **211**, 2105–2115. (doi:10.1242/jeb.016204)

29. Raible DW, Kruse GJ. 2000 Organization of the lateral line system in embryonic zebrafish. *J. Comp. Neurol.* **421**, 189–198. (doi:10.1002/(SICI)1096-9861(20000529)421:2<189::AID-CNE5>3.0.CO;2-K)

30. McHenry MJ, van Netten SM. 2007 The flexural stiffness of superficial neuromasts in the zebrafish (*Danio rerio*) lateral line. *J. Exp. Biol.* **210**, 4244–4253. (doi:10.1242/jeb.009290)

31. Carton AG, Montgomery JC. 2004 A comparison of lateral line morphology of blue cod and torrent fish: two sandperches of the family Pinguipedidae. *Environ. Biol. Fish.* **70**, 123–131. (doi:10.1023/B:EBFI.0000029340.57735.f8)

32. Schmitz A, Bleckmann H, Mogdans J. 2014 The lateral line receptor array of cyprinids from different habitats. *J. Morphol.* **275**, 357–370. (doi:10.1002/jmor.20219)

33. Jorde K, Schneider M, Peter A, Zöllner F. 2001 Fuzzy based models for the evaluation of fish habitat quality and instream flow assessment. In *Proc. of the 2001 Int. Symp. on Environmental Hydraulics*, pp. 27–28. Beijing, China: IAHR.

34. Steffler P, Blackburn J. 2002 *River2D - two-dimensional depth averaged model of river hydrodynamics and fish habitat*, 119 p. Edmonton, Canada: University of Alberta.

35. Zhu Q, Wolfgang MJ, Yue DKP, Triantafyllou MS. 2002 Three-dimensional flow structures and vorticity control in fish-like swimming. *J. Fluid Mech.* **468**, 1–28. (doi:10.1017/S002211200200143X)

36. Klein A, Bleckmann H. 2015 Function of lateral line canal morphology. *Integr. Zool.* **10**, 111–121. (doi:10.1111/1749-4877.12101)

37. Ristroph L, Liao JC, Zhang J. 2015 Lateral line layout correlates with the differential hydrodynamic pressure on swimming fish. *Phys. Rev. Lett.* **114**, 018102. (doi:10.1103/PhysRevLett.114.018102)

38. Herzog H, Steltenkamp S, Klein A, Tätzner S, Schulze E, Bleckmann H. 2015 Micro-machined flow sensors mimicking lateral line canal neuromasts. *Micromachines* **6**, 1189–1212. (doi:10.3390/mi6081189)

39. Chambers LD, Akanyeti O, Venturelli R, Jezov J, Brown J, Kruusmaa M, Fiorini P, Megill WM. 2014 A fish perspective: detecting flow features while moving using an artificial lateral line in steady and unsteady flow. *J. R. Soc. Interface* **11**, 20140467. (doi:10.1098/rsif.2014.0467)

40. Goulet J, Engelmann J, Chagnaud BP, Franosch JMP, Suttner MD, van Hemmen JL. 2008 Object localization through the lateral line system of fish: theory and experiment. *J. Comp. Physiol. A* **194**, 1–17. (doi:10.1007/s00359-007-0275-1)

41. Rapo MA, Jiang H, Grosenbaugh MA, Coombs S. 2009 Using computational fluid dynamics to calculate the stimulus to the lateral line of a fish in still water. *J. Exp. Biol.* **212**, 1494–1505. (doi:10.1242/jeb.026732)

42. Windsor SP, Tan D, Montgomery JC. 2008 Swimming kinematics and hydrodynamic imaging in the blind Mexican cave fish (*Astyanax fasciatus*). *J. Exp. Biol.* **211**, 2950–2959. (doi:10.1242/jeb.020453)

43. Windsor SP, Norris SE, Cameron SM, Mallinson GD, Montgomery JC. 2010 The flow fields involved in hydrodynamic imaging by blind Mexican cave fish (*Astyanax fasciatus*). Part I: open water and heading towards a wall. *J. Exp. Biol.* **213**, 3819–3831. (doi:10.1242/jeb.040741)

44. Windsor SP, Norris SE, Cameron SM, Mallinson GD, Montgomery JC. 2010 The flow fields involved in hydrodynamic imaging by blind Mexican cave fish (*Astyanax fasciatus*). Part II: gliding parallel to a wall. *J. Exp. Biol.* **213**, 3832–3842. (doi:10.1242/jeb.040790)

45. Windsor SP, McHenry MJ. 2009 The influence of viscous hydrodynamics on the fish lateral-line system. *Integr. Comp. Biol.* **49**, 691–701. (doi:10.1093/icb/icp084)

46. Chagnaud BP, Bleckmann H, Hofmann MH. 2008 Lateral line nerve fibers do not code bulk water flow direction in turbulent flow. *Zoology* **111**, 204–217. (doi:10.1016/j.zool.2007.07.009)

47. Webb JF. 1989 Neuromast morphology and lateral line trunk canal ontogeny in two species of cichlids: an SEM study. *J. Morphol.* **202**, 53–68. (doi:10.1002/jmor.1052020105)

48. Metscher BD. 2009 MicroCT for comparative morphology: simple staining methods allow high-contrast 3D imaging of diverse non-mineralized animal tissues. *BMC Physiol.* **9**, 11. (doi:10.1186/1472-6793-9-11)

49. Schulz-Mirbach T, Heß M, Metscher BD, Ladich F. 2013 A unique swim bladder-inner ear connection in a teleost fish revealed by a combined high-

resolution microtomographic and three-dimensional histological study. *BMC Biol.* **11**, 75. (doi:10.1186/1741-7007-11-75)

50. Deary AL, Metscher B, Brill RW, Hilton EJ. 2016 Shifts of sensory modalities in early life history stage estuarine fishes (Sciaenidae) from the Chesapeake Bay using X-ray micro computed tomography. *Environ. Biol. Fish.* **99**, 361–375. (doi:10.1007/s10641-016-0479-8)

51. Wu C. 2013 Towards linear-time incremental structure from motion. In *Int. Conf. on 3D Vision 2013*, pp. 127–134. New York, NY: IEEE.

52. Lowe DG. 2004 Distinctive image features from scale-invariant keypoints. *Intern. J. Comp. Vision* **60**, 91–110. (doi:10.1023/B:VISI.0000029664.99615.94)

53. Wu C, Agarwal S, Curless B, Seitz SM. 2011 Multicore bundle adjustment. In *Int. Conf. on Computer Vision and Pattern Recognition 2011*, pp. 3057–3064. New York, NY: IEEE.

54. Schneider C, Rasband W, Eliceiri K. 2012 NIH image to ImageJ: 25 years of image analysis. *Nat. Methods* **9**, 671–675. (doi:10.1038/nmeth.2089)

55. Limaye A. 2012 Drishti: a volume exploration and presentation tool. *Proc. SPIE* **8506**, 85060X. (doi:10.1117/12.935640)

56. Kumar P, Ziegler A, Ziegler J, Uchanska-Ziegler B, Ziegler A. 2008 Grasping molecular structures through publication-integrated 3D models. *Trends Biochem. Sci.* **33**, 408–412. (doi:10.1016/j.tibs.2008.06.004)

57. Kumar P, Ziegler A, Grahn A, Hee CS, Ziegler A. 2010 Leaving the structural ivory tower, assisted by interactive 3D PDF. *Trends Biochem. Sci.* **35**, 419–422. (doi:10.1016/j.tibs.2010.03.008)

58. Ziegler A, Mietchen D, Faber C, von Hausen W, Schöbel C, Sellerer M, Ziegler A. 2011 Effectively incorporating selected multimedia content into medical publications. *BMC Med.* **9**, 17. (doi:10.1186/1741-7015-9-17)

59. Engelmann J, Hanke W, Bleckmann H. 2002 Lateral line reception in still- and running water. *J. Comp. Physiol. A* **188**, 513–526. (doi:10.1007/s00359-002-0326-6)

60. Chagnaud BP, Hofmann MH, Mogdans J. 2007 Responses to dipole stimuli of anterior lateral line nerve fibres in goldfish, *Carassius auratus*, under still and running water conditions. *J. Comp. Physiol. A* **193**, 249–263. (doi:10.1007/s00359-006-0184-8)

61. Herzog H, Klein B, Ziegler A. 2017 Form and function of the lateral line revealed using three-dimensional imaging and computational fluid dynamics. *MorphoBank Project* 2542. (doi:10.7934/P2542)

62. Sapède D, Gompel N, Dambly-Chaudière C, Ghysen A. 2002 Cell migration in the postembryonic development of the fish lateral line. *Development* **129**, 605–615.

63. Chiu LL, Cunningham LL, Raibel DW, Rubel EW, Ou HC. 2008 Using the zebrafish lateral line to screen for ototoxicity. *J. Assoc. Res. Otolaryngol.* **9**, 178–190. (doi:10.1007/s10162-008-0118-y)

64. van Trump WJ, Coombs S, Duncan K, McHenry MJ. 2010 Gentamicin is ototoxic to all hair cells in the fish lateral line system. *Hear. Res.* **261**, 42–50. (doi:10.1016/j.heares.2010.01.001)

65. Bird N, Webb J. 2014 Heterochrony, modularity, and the functional evolution of the mechanosensory lateral line canal system of fishes. *EvoDevo* **5**, 21. (doi:10.1186/2041-9139-5-21)

66. Berquist RM *et al.* 2012 The digital fish library: using MRI to digitize, database, and document the morphological diversity of fish. *PLOS ONE* **7**, e34499. (doi:10.1371/journal.pone.0034499)

67. Ziegler A, Mueller S. 2011 Analysis of freshly fixed and museum invertebrate specimens using high-resolution, high-throughput MRI. *Methods Mol. Biol.* **771**, 633–651. (doi:10.1007/978-1-61779-219-9_32)

68. Ziegler A, Kunth M, Mueller S, Bock C, Pohmann R, Schröder L, Faber C, Giribet G. 2011 Application of magnetic resonance imaging in zoology. *Zoomorphology* **130**, 227–254. (doi:10.1007/s00435-011-0138-8)

69. Fernández R, Kvist S, Lenihan J, Giribet G, Ziegler A. 2014 *Sine systemate chaos?* A versatile tool for earthworm taxonomy: non-destructive imaging of freshly fixed and museum specimens using micro-computed tomography. *PLOS ONE* **9**, e96617. (doi:10.1371/journal.pone.0096617)

70. Sigl R, Imhof H, Settles M, Laforsch C. 2013 A novel, non-invasive and *in vivo* approach to determine morphometric data in starfish. *J. Exp. Mar. Biol. Ecol.* **449**, 1–9. (doi:10.1016/j.jembe.2013.08.002)

71. Vischer HA. 1990 The morphology of the lateral line system in three species of Pacific cottoid fishes occupying disparate habitats. *Experientia* **46**, 244–250. (doi:10.1007/BF01951754)

72. Lannoo MJ. 1987 Neuromast topography in anuran amphibians. *J. Morphol.* **191**, 115–129. (doi:10.1002/jmor.1051910203)

73. van Netten SM. 2006 Hydrodynamic detection by cupulae in a lateral line canal: functional relations between physics and physiology. *Biol. Cybern.* **94**, 67–85. (doi:10.1007/s00422-005-0032-x)

74. Görner P. 1963 Untersuchungen zur Morphologie und Elektrophysiologie des Seitenlinienorgans vom Krallenfrosch (*Xenopus laevis* Daudin). *Z. Vergl. Physiol.* **47**, 316–338. (doi:10.1007/BF00298039)

75. Coombs S, Braun CB, Donovan B. 2001 The orienting response of Lake Michigan mottled sculpin is mediated by canal neuromasts. *J. Exp. Biol.* **204**, 337–348.

76. Hassan ES. 1985 Mathematical analysis of the stimulus for the lateral line organ. *Biol. Cybern.* **52**, 23–36. (doi:10.1007/BF00336932)

77. Hassan ES. 1992 Mathematical description of the stimuli to the lateral line system of fish derived from a three-dimensional flow field analysis. *Biol. Cybern.* **66**, 443–452. (doi:10.1007/BF00197725)

78. Teyke T. 1988 Flow field, swimming velocity and boundary layer: parameters which affect the stimulus for the lateral line organ in blind fish. *J. Comp. Physiol. A* **163**, 53–61. (doi:10.1007/BF00611996)

79. Denton E, Gray J. 1989 Some observations on the forces acting on neuromasts in fish lateral line canals. In *The mechanosensory lateral line: neurobiology and evolution* (eds S Coombs, P Görner, H Münz), pp. 229–246. New York, NY: Springer.

80. Guidelines for the treatment of animals in behavioural research and teaching. 2012. *Anim. Behav.* **83**, 301–309. (doi:10.1016/j.anbehav.2011.10.031)